System Level Analysis of Millimetre-wave GaN-based MIMO Radar for Detection of Micro Unmanned Aerial Vehicles

(Article begins on next page)

19 April 2024

# System Level Analysis of Millimetre-wave GaN-based MIMO radar for detection of micro unmanned aerial vehicles

**A. Cidronali[1], M. Passafiume[1], P. Colantonio[2], G. Collodi[1] , C. Florian[3], G. Leuzzi[4], M. Pirola[5], C. Ramella[5], A. Santarelli[3], and P. Traverso[3]**

[1]Department of Information Engineering, University of Florence, Italy
[2]Department of Electronics Engineering, University of Rome, Tor Vergata, Italy
[3]Department of Electrical, Electronic and Information Engineering, University of Bologna, Italy
[4]Department of Industrial and Information Engineering, University of L'Aquila, Italy
[5]Department of Electronics and Telecommunications, Polytechnic of Turin, Italy

**Abstract**— The detection of Unmanned Aerial Vehicles (UAVs) of micro/nano dimensions, is becoming a hot topic, due to their large diffusion, and represents a challenging task from both the system architecture and components point of view. The Frequency Modulated Continuous Wave (FMCW) radar architecture in a Multi-Input Multi-Output configuration has been identified as the most suitable solution for this purpose, due to both its inherent short-range detection capability and compact implementation. This paper describes the operation and technology challenges inherent to the development of a millimeter-wave FMCW MIMO radar for small UAVs detection. In particular it analyzes the sub-systems specifications and the expected system performance with respect to a chip set designed and developed in GaN at 37.5 GHz applications.

## 1. INTRODUCTION

The detection of Unmanned Aerial Vehicles (UAVs) of micro/nano dimensions, is becoming a notable topic, due to their large diffusion, and represents a challenging task. The Frequency Modulated Continuous Wave (FMCW) radar architecture, cfr. Fig. 1, has been identified as the most suitable solution for this purpose [1], due to its inherent short-range detection capability. By exploiting the properties of the echo signal reflected by the UAV, which are mainly related to small radar cross section (RCS) and significantly affected by the micro-Doppler effect [2], the UAVs classification appears to be feasible. In order to improve detection range and resolution, millimeter-wave technologies are suitable due to their high carrier frequencies and related wide bandwidth, supported by high transmitted power, along with receiver low noise figure and large dynamic range.

This paper analyzes the feasibility and expected performance of a radar front-end system, operating at 37.5 GHz, with 1.5 GHz bandwidth, based on GaN technology. In particular, the proposed system level analysis considers the effects of the main sub-system blocks actual characteristics, designed by the Gallium Nitride on Silicon substrate (GaN-on-Si) process D01GH available from OMMIC foundry, these are the high-power amplifier (HPA); the low noise amplifier (LNA), and the mixer. The systems consider also the characteristics of a suitable planar antenna. The system radar architecture considered in this study corresponds to the class of co-located Multiple-Input Multiple-Output (MIMO) and for this purpose an appropriate antenna was considered in the system simulator, along with the signal level processing suitable for the range and angle estimation.
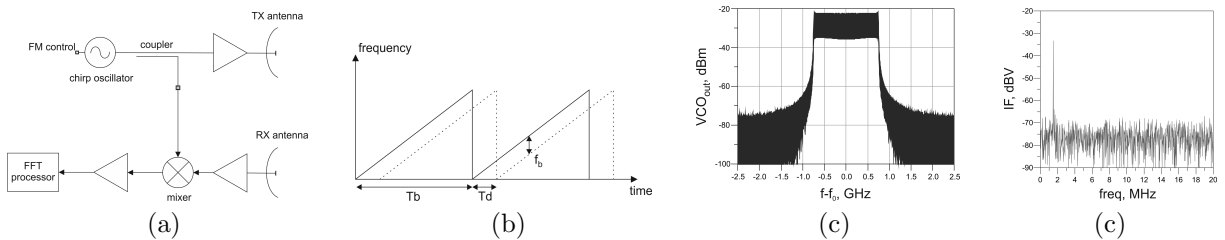


Figure 1: Schematic representation of a FMCW radar: (a) simplified architecture, (b) transmitted and received frequency-modulated signals, (c) transmitted signal spectrum, (d) received signal spectrum.

## 2. REVIEW OF FMCW RADAR PRINCIPLE OF OPERATION

Frequency Modulated Continuous Wave (FMCW) radars adopt a transceiver in which the same signal synthesizer drives both the transmitter and the frequency down-conversion in the receiver, thus permitting an effective coherence between the transmitted and received signals. With reference to Fig. 1, the CW signal is modulated in frequency to produce a linear chirp, which is transmitted toward the target. The signal echo received with a $T_d$ delay, is down-converted by using the transmitted signal as reference, to produce a beat signal at a frequency $f_b$ (hereinafter referred to as $F_{IF}$), which is proportional to the round-trip time $T_d = 2 \cdot D/c$, being $D$ the target distance and $c$ the light velocity.

### 2.1. Range estimation in FMCW radar architectures

For an analytical discussion of the basic FMCW operation, the linear frequency modulation that generates the transmitted chirp is assumed to be: $\omega = A_b \cdot t$. From this it results the transmitted signal

$$v_{FM}(t) = A_c cos\left(\omega_c t + \frac{A_b}{2}t^2\right) \tag{1}$$

A portion of the transmitted signal is extracted by the transmitter chain by a directional coupler and then adopted as local oscillator in the receiver chain, this permits the coherent mixing with the returned echo. The latter is a delayed replica of the former, by the round trip time $T_d$, cfr. Fig. 1

$$v_{FM}(t - T_d) = A_c cos\left(\omega_c(t - T_d) + \frac{A_b}{2}(t - T_d)^2\right) \tag{2}$$

Assuming an ideal mixing, by calculating the multiplication between (1) and (2), we have

$$v_{IF}(t) = \frac{A_c^2}{2}\left[cos\left((2\omega_c - A_b T_d)t + A_b t^2 + \frac{A_b}{2}T_d^2 - \omega_c T_d\right) + cos\left(A_b T_d t + \omega_c T_d - \frac{A_b}{2}T_d^2\right)\right] \tag{3}$$

In (3), the first cosine term describes a linearly increasing FM signal, i.e. the chirp, at about twice the carrier frequency with a phase shift that is proportional to the delay time $Td$. This term is generally filtered out. The second cosine term describes a beat signal at a fixed frequency

$$f_{IF} = \frac{A_b}{2\pi}T_d \tag{4}$$

thus the beat frequency is directly proportional to the delay time, having fixed the ramp slope, $A_b$.

Figure 1 shows an example of transmitted spectrum and the corresponding IF output signal spectrum that contains the constant frequency components at $f_{IF}$. For a chirp duration of $Tb$ seconds, the spectrum of the IF signal will be resolvable to an accuracy of $2/Tb$ Hz, which correspond to the main lobe width of IF spectrum, assuming that $Tb >> Td$. The rate of frequency modulation, $A_b$, in the linear case is constant and equal to the frequency bandwidth, $B_W$ divided by the time $Tb$. From the basics of radar, the round trip time $Td$ to the target and back can be written in terms of the range as

$$T_d = \frac{2R}{c} \tag{5}$$

which can be substituted into (4) to give the classical FMCW formula that relates the IF frequency and the target range

$$f_{IF} = \frac{B_W}{T_d}\frac{2R}{c} \tag{6}$$

### 2.2. Range Resolution

Solving for the range, R, from (6) leads to

$$R = \frac{T_d c}{2B_W}f_{IF}. \tag{7}$$

From (7) can be easily calculated the range resolution by differentiating

$$\delta R = \frac{T_d c}{2B_W}\delta f_{IF} \tag{8}$$

The resolution, $\delta R$, in terms of $\delta f_{IF}$ is assumed to be $\delta f_{IF} = 1/T_b$, thus the range resolution becomes

$$\delta R = \frac{c}{2B_W} \tag{9}$$

## 3. NONIDEALITIES IN FMCW RADAR

In this section we discuss some of the main impairments that frequently occur in millimeter wave FMCW radar, which are included in the system simulation that follows, namely the transmitter phase noise and the transmitter power leakage to the receiver, [1].

### 3.1. Effects of VCO Phase Noise

If the phase noise contribution is included in the IF signal equation, (3) it leads to

$$v_{IF}^{pn}(t) = \frac{A_c^2}{2}cos\left[A_bT_dt + \left(\omega_cT_d - \frac{A_b}{2}T_d^2\right) + \phi(t) - +\phi(t - T_d)\right], \tag{10}$$

we can then observe that the process of obtaining the IF frequency involves the difference between two signals, one of which represents the delayed version of the other, by the function

$$H(j\omega) = 1 - e^{-j\omega T_d} \tag{11}$$

taking the squared magnitude we obtain

$$|H(j\omega)|^2 = 2(1 - cos(\omega T_d)). \tag{12}$$

The IF power density spectrum for a synthesizer phase noise of $S_{VCO}(f)$ it is thus the product of the (12) and the noise power spectrum

$$S(f) = 2S_{VCO}(f)(1 - cos(\omega T_d)). \tag{13}$$

The noise power relative to the carrier at an offset $\Delta f$ from the carrier in dBc/Hz results

$$N(\Delta f) = 10 \cdot log_{10}\left[2S_{VCO}(\Delta f)(1 - cos(\Delta f T_d))\right] \tag{14}$$

In presence of transmitter to receiver power leakage, the round-trip time is replaced by its equivalent path length difference $T_d = \Delta R/c$. For the case of path difference of about 100 mm, it results that the attenuation of the correlated phase noise is about 76 dB at the offset frequency of 100 kHz. Hence, if the oscillator power is $P_T$ dBm and the leakage is $L_{leak}$ dB, then the power levels must be scaled by $P_T - L_{leak}$ to obtain the actual noise power density

$$Pn(\Delta f) = P_T - N(\Delta f) - L_{leak} - 10 \cdot log(B_W). \tag{15}$$

From this conclusion it is clear that the FMCW radar performance in term of signal to noise ratio, is impaired by the synthetizer phase noise, thus increasing the transmitter power raises the noise floor proportionally and no improvement in performance is to be expected. This impairment is common to other communication technologies that operate according to the full-duplex homodyne principle, [4].

### 3.2. Transmitter Leakage Power

From the consideration described in Section 3.1, the only way to increase the range performance of the FMCW radar configuration consists in using an oscillator that has superior phase noise characteristics or decrease the magnitude of the leakage signal. Obviously, the back-scattered signal should be in the dynamic range of the receiver. A technique suitable for the reduction of the leakage signal, consists in increase the distance between transmitter and receiving antenna. Nevertheless this approach hardly permits to reach values better than 40 dB across wide bandwidth.

The mitigation of the transmitter to receiver leakage is achieved by an adaptive vector modulator based architecture, aimed at providing an auxiliary signal to be injected into the receiver chain capable to cancel the leakage, [5]. The architecture of the FMCW radar in which the transmitter leakage canceller is included in shown in Fig. 2. The primary advantage of the adaptive cancellation technique is that it can maintain the lowest leakage irrespective of the transmitter frequency, and hence limitations to the swept bandwidth are not an issue. It's effect on the FMCW radar operation is beyond the aim of the present paper.
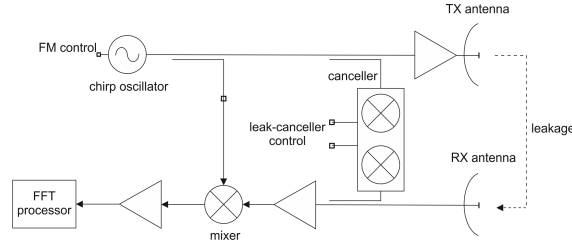
Figure 2: The schematic architecture of a FMCW radar including a transmitter leakeage canceller

## 4. THE MIMO RADAR CONCEPT

While the mechanism of radar based on the phased array is well known, the recent combination of phased array with the multiple-input/multiple-output (MIMO) concept [6]–[8] has led to an emerging area where lower cost and higher performance can be achieved simultaneously, making MIMO phased array radar an attractive candidate for imaging applications. The MIMO radar
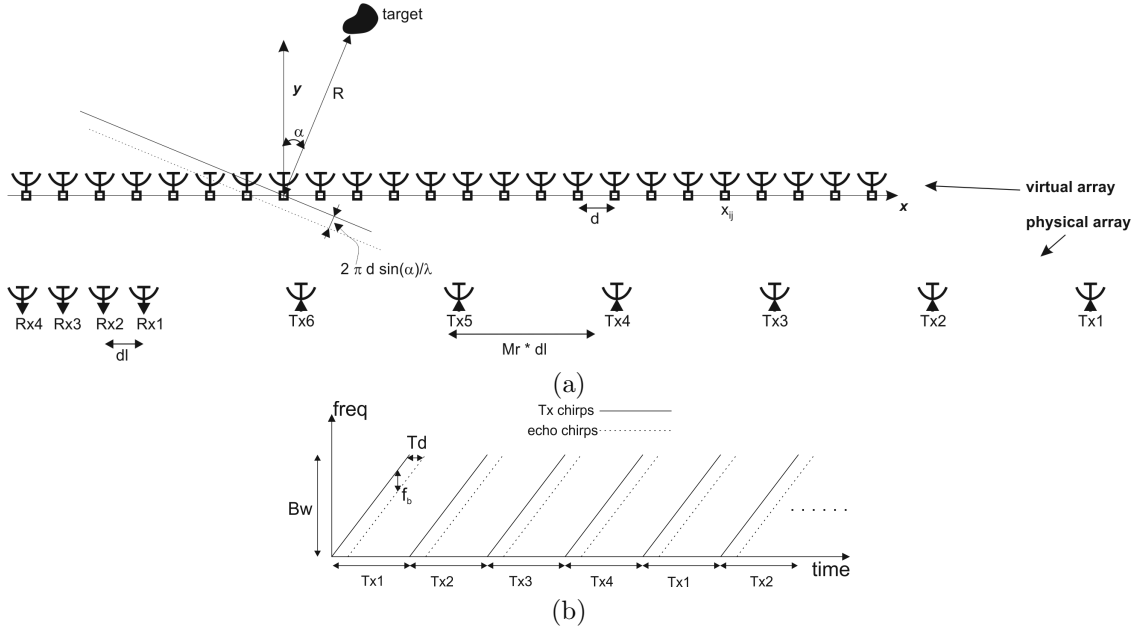


Figure 3: MIMO concepts: (a) virtual vs physical array (b) timing for four TX elements array].

consists of multiple antenna elements in both signal transmission and reception, Fig. 3. For MIMO radar with $M_T$ transmit elements and $M_R$ receive elements, there are $M_T \cdot M_R$ distinct propagation paths from the TX array to the RX array, with only $M_T + M_R$ antenna elements. Incoherence between the TX channels is generally achieved by exploiting time division multiplexing (TDM). According to conventional antenna array theory the angular resolution is proportional to the aperture size of the antenna array, this leads to use a MIMO configuration with high number of virtual elements to increase the aperture. A conventional used TDM scheme is also shown in Fig. 3 for four transmitters, which are active in an alternating way. Hence, the chirp repetition time of the same transmit antenna is augmented by the number of different transmit antenna $M_T = 4$ , in this example. Figure 3 shows an example array with 6 TX and 4 RX antenna elements, synthesizing a uniform linear array of 24 virtual elements. The placement consists of a symmetrical linear arrangement of the TX and RX elements. Assuming far field operations, the signal propagation from a TX elements $x_i^{TX}$ to a point scatterer $\mathbf{p}$ plus reflection path from $\mathbf{p}$ to RX elements can be approximated by the two-way path, P between the corresponding *virtual element* $x_{ij} = \left( x^{RX} + x^{TX} \right) /2$, and the scatterer $\mathbf{p}$

$$P_{ij}\left(p\right) = \left|\mathbf{p} - x_i^{TX}\right| + \left|\mathbf{p} - x_j^{RX}\right| \approx 2\left|\mathbf{p} - x_{ij}\right| \tag{16}$$

The technique to arrange a MIMO array with non-overlapping equally spaced elements is, [9]

1. given the TX-RX virtual element spacing, $d$,

2. the inter-element spacing in either group of the TX array needs to be $d_{RX} = 2d$,

3. the inter-element spacing in the RX array shall be $d_{TX} = M_R \cdot 2d$,

According to these requirements, a virtual linear array of $M_T \cdot M_R$ elements separated by $d$ can be formed in signal processing. Assuming that the far field condition is fulfilled, the the two-way delay between a virtual element at $x_{ij}$ and a scatterer at range R with an azimuthal angle $\theta$ can be expressed as

$$\Delta t_{ij} = \frac{2R}{c} + \frac{2x_{ij} sin\theta}{c} \tag{17}$$

the phase term in (3) reflects the arrival angle of the echo, which can be found by *digital beamforming* with the appropriate steering vectors. It contains a linear $2\pi f_c \Delta_{ij}$, and a squared component $\pi A_b \Delta_{ij}^2$ of the delays. It shall be noted that, for a scatterer within the detectable range of the radar, the squared component is nearly constant for all the virtual channels. The deramped phase term can therefore be expressed as the sum of a phase component dependent on the element coordinates and a constant dependent on the scatterer range

$$\phi = 2\pi f_c \Delta_{ij} - \pi Ab \Delta_{ij}^2 = 2\pi f_c \frac{2x_{ij} sin(\theta)}{c} + 2\pi f_c \frac{2R}{c} - \pi A_b \Delta t_{ij}^2 = 4\pi \frac{2x_{ij} sin(\theta)}{\lambda} + C \tag{18}$$

It is introduced a steering vector suitable to estimate the relative angle of the reflected signal, this is given by the product of the steering vector for the TX array and the steering vector of the RX array. The former is provided by

$$a_i^{tx}(\theta) = exp\left(-j2\pi \frac{2x_i^{tx} sin(\theta)}{\lambda}\right); i = 1, 2, \cdots, Mt \tag{19}$$

while for the receiver

$$a_j^{rx}(\theta) = exp\left(-j2\pi \frac{2x_i^{rx} sin(\theta)}{\lambda}\right); i = 1, 2, \cdots, Mr \tag{20}$$

assuming that $x_{ij} = \left(x_i^{tx} + x_i^{rx}\right)/2$, the virtual array steering vector is

$$a_{ij}(\theta) = a_j^{rx}(\theta) \otimes a_i^{tx}(\theta) = exp\left(-j2\pi \frac{\left(x_i^{rx} + x_j^{tx}\right) sin(\theta)}{\lambda}\right) = exp\left(-j4\pi \frac{x_{ij} sin(\theta)}{\lambda}\right) \tag{21}$$

with $i = 1...M_R$ and $j = 1...M_T$. The virtual array $x_{ij}$ is to be considered as an effective array of $M_R \cdot M_T$ receivers at the distance $d_l$ each other. In order to synthesize the total number of $M_R \cdot M_T$ MIMO channels, the signal processing is to be able to differentiate the TX channels and separate the time samples according to their originating TX sources. A simple yet reliable method is time division; switching the TX channels on or off for radiation at different time slots, the concept is illustrated in Fig. 3. With this switching scheme the TX elements are activated in turn while the RX elements are receiving signals coherently. Reception of signals for the $M_T$ slots makes a cycle. The total $M_R \cdot M_T$ channels of signals are found and an image can be produced when the reflected signals from all the TX slots are received. If the chirp duration is much longer than the two-way propagation delay ($T_d = 2R_{max}/c << Tc$), the range and angle information carried by the received signals can be retrieved at the resolutions defined by (9) and $2\pi/(M_R \cdot M_T - 1)$. Desired resolution defines the chirp duration which is usually as longer as possible to deliver greater received echo energy. Nevertheless, target velocity imposes a limitation as the change of radian frequency $\Delta f_{IF}$ over one chirp duration, $Tc$, should not be greater than the frequency resolution $1/Tc$.

## 4.1. Digital beamforming

Having defined the virtual array of receiving elements, the radar image is achieved straightforwardly in radial coordinate. Assuming an ideal scenario with a target at the distance, R, with azimuth $\theta$, the FFT elaboration at each receiver provides a spectrum with only one maximum at $\omega_{IF}$ same amplitude, A, and phase depending on $\theta$

$$a_{ij}(\theta) = A \cdot e^{(-j\omega_{IF} t)} \cdot e^{\left(-j2\pi \cdot \frac{sin(\theta)}{\lambda} \cdot ij \cdot dl\right)} \tag{22}$$

where the positions $x_{ij}$ are defined according to Fig. 3, which raprasents a linear array of elements distributed uniformly with a distance $dl$. Let's now consider to apply a second FFT operator to (22) where the discrete variable of integration is $ii \cdot dl$. This second FFT is thus computed across the virtual element and thus return a spectrum composed by an only raw at the 'frequency' $sin(\theta)/\lambda$. This term can be easily inverted to achieve the direction-of-arrival $\theta$.

From this results the condition

$$\left| \frac{sin(\theta)}{\lambda} \cdot dl \right| \leq 1/2 \tag{23}$$

that is required to avoid spectrum fold overlapping; in the case of a maximum observable angle $|\theta| = \pi/2$ it results $dl = \lambda/2$. The angular resolution $\Delta\theta$ in radians at a given angle $\theta$, observed by the virtual array with the aforementioned beamforming is dependent on the effective aperture, $Ae$, of the virtual array.

$$\Delta\theta = \frac{\lambda}{2A_e} = \frac{\lambda}{2\left(M_T M_R - 1\right) dl \cdot \cos\left(\theta\right)} \tag{24}$$

For instance the resolution at boresight is $16^o$ and $1.8^o$ with respectively 8 and 64 virtual elements; the cross range resolution can be approximated to $\Delta R \approx \Delta\theta \cdot R$.
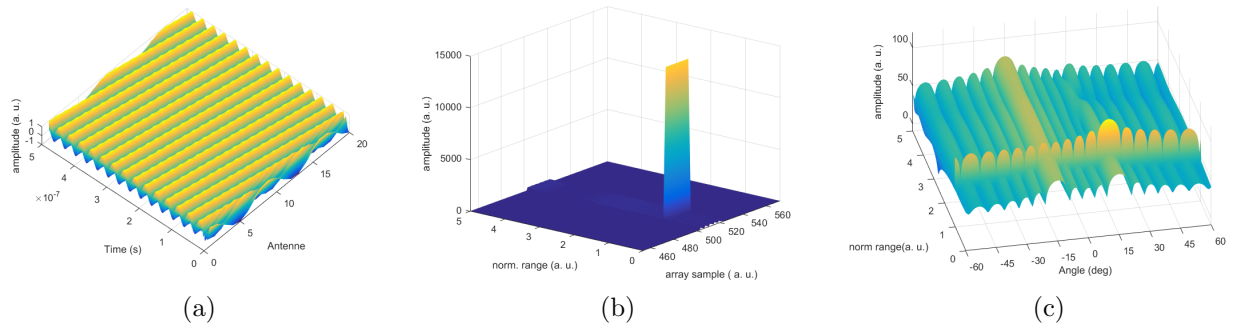


Figure 4: Processing steps in the MIMO range and angle estimation. (a) time domain signal across the receivers, (b) first FFT results, (c) second FFT across the array.

In Fig. 4 are reported the three steps of a MIMO FMCW radar imaging; assuming an experiment where a target is at $\theta = 15$ degree, while target distance and the other parameters of the signal are normalized for convenience. The first process step consists of the acquisition of the deramped time domain signal according to the (22), it is shown in Fig. 4a, where a surface plot depicts the plane wave incident to the virtual array of 20 elements. The second step consists of the FFT signal process which is needed to estimate the range; because the assumption of far field the result consists of a peak on the spectrum at the same frequency for each receiver, as shown in Fig. 4b where the conversion frequency to distance is already computed according to (7). The next step consists on a second FFT process across the virtual array elements in order to estimate the angle of arrival accorsing to the (22), for this purpose a zero-padding procedure is implemented to increase the apparent resolution. The result of this second step is also shown in Fig. 4c, where the angular distortion introduced by the term $\frac{sin(\theta)}{\lambda}$ is visible at the limit of the observable range; in the figure the correct estimation of $\theta$ is clearly evident.

## 5. SYSTEM ARCHITECTURE

The system analysis that follow consider two MIMO radar sizes, the firs one assumes $M_T = 4$ and $M_R = 16$ while the second $M_T = 2$ and $M_R = 2$, for both the configuration the system architecture is similar and for the second case it is illustrated in Fig. 5. For both the cases of study the specifications are reported in Table 1.

The architecture considers the chirp signal fed by a single-pole $M_T$-trough switch to the $M_T$ power amplifiers sequentially and according to the time ramp of duration $T_b$. The switch is synchronized with the signal source and connect each TX element sequentially so a full scan lasts for $T_c = 4$ ms. The chirp rate is estimated for operating range and the expected velocity of the targets. Echo signals are received by the $M_R$ RX elements simultaneously and deramp processing is applied directly beyond reception of the signals by means of an RF single-ended mixer, which

mixes the transmitted chirp with the received echoes and producing IF signals whose frequencies are proportional to range of targets (cf. Section 2). The IF signals are firstly high-pass filtered to compensate for the range dependent propagation loss before being sampled simultaneously by a $M_R$-channel ADC at a rate of at least 100 MS/s. The main blocks specification are defined as in Table 2, which are calculated by the design principles described in this document.

## 5.1. Basic radar equations

The transmitted power density that strikes the target, at the distance R, is given by: $P_R = P_T \cdot G_T / \left(4\pi R^2\right)$, where Gt is the transmitter antenna gain and $P_T$ the transmitted power. Some of that energy will be reflected in various directions and some will be reradiated back to the radar system. The amount of incident power density that is reradiated back to the radar is a function of the target RCS or $\sigma$ of the target; the RCS has units of area and is a measure of target size, as seen by the radar.

In the present analysis we consider the Swerling IV RCS model where the $\sigma$ varies according to a Chi-squared probability density function (PDF) with four degrees of freedom, with and average value $\sigma_{av}$. This PDF approximates the scattering from an object with one larger scattering surface with several other smaller scattering surfaces; the $\sigma$ is constant through a single scan $Tb$.

$$p(\sigma) = \frac{4\sigma}{\sigma_{av}^2} e^{-\frac{2\sigma}{\sigma_{av}}} \tag{25}$$

The system analysis consider a coherent variation of $\sigma$ from chirp to chirp. Under this assumption the power density returned to the radar is the product of two terms

$$P_R = \frac{P_T G_T G_R \lambda^2 \sigma_{av}}{(4\pi)^3 R^4} \tag{26}$$

with $G_R$ the receiver array antenna gain.

## 5.2. Process gain

In this application the actual IF signal of interest occupies a smaller bandwidth, say $B_W$, which is less than the actual Nyquist bandwidth that is $F_{sampling}/2$. If digital filtering is used to filter out noise components outside the bandwidth $B_W$, then process gain could be included in the budget link to account for the resulting increase in signal to noise ratio (SNR) as

$$SNR = 6.02 \cdot ENOB + 1.76\,dB + 10log_{10}\frac{f_S}{2 \cdot B_W} \tag{27}$$

where ENOB stands for the ADC effective number of bit. The process of sampling a signal at a rate, $f_S$ which is greater than twice its bandwidth is referred to as oversampling.
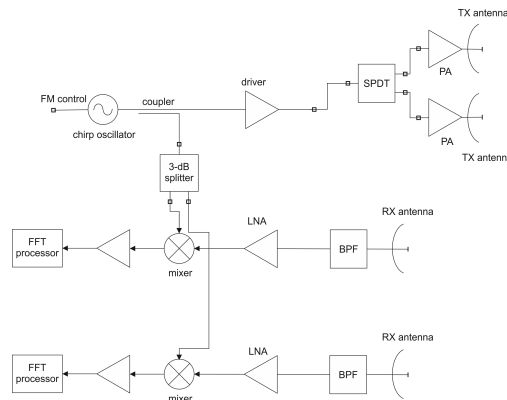


Figure 5: The schematic architecture of a 2x2 MIMO FMCW radar

Under the specification provided in the Table 1, we defined the subsystem level specifications that drive the design of each system part and the operation of the MIMO system; these are provided in the Table 2 and are referenced for the system analysis that follows. Before proceeding further we report the description of the main blocks which were designed according to this specific application.

Table 1: UAV detection test case

| | |
|---|---|
| center frequency, GHz | 37.5 |
| bandwidth, GHz | 1.5 |
| distance, m | 1000 |
| $\sigma_{av}, m^2$ | 0.1 |
| velocity, km/h | 100 |

Table 2: MIMO radar specifications for UAV detection

| | | | |
|---|---|---|---|
| output power, dBm | 36.8 | process gain, dB | 53 |
| antenna RX gain, dB | 18 | input 1-dB compression LNA, dB | 0 |
| antenna TX gain, dB | 12 | LNA dynamic range, dB | 91.8 |
| chirp time, ms | 2 | ENOB | 15.3 |
| receiver noise figure, dB | 2 | TX-RX isolation, dB | 36.8 |
| post-processing SNR, dB | 10 | radar equation, dB | -184.7 |
| ADC sampling, MHz | 100 | LO phase noise, dBm/Hz at 1MHz | -108 |
| IF bandwidth, MHz | 10 | SNR, dB | 10 |

The semiconductor process adopted for the development of the LNA, the HPA and the mixer is based on the Gallium Nitride (GaN) High Electron Mobility Transistor (HEMT) with 100 nm of gate length and capable to provide 2.5 W/mm power density at 30 GHz with 180 GHz maximum frequency.

### 5.3. The power amplifier

According to the specifications provided in the Table 2, a 3-stage power amplifier (PA) was designed. To ensure wide bandwidth (5 GHz) and good linearity performance a class-AB combined solution has been adopted, [10]–[12]. The power stage of the PA is composed of 4 parallel GaN HEMTs for a total periphery of 1.6 mm and it is capable of providing 38 dBm of peak output power in the entire design bandwidth of 35 - 40 GHz. Then two gain stages are added, counting in total 3 more transistors, to achieve a total power gain above 15 dB. Each stage is biased independently from the other to allow some bias tuning for performance optimization. The layout of the circuit is shown in Fig. 6a, while the output power, power gain and power added efficiency are provided in Fig. 6b.
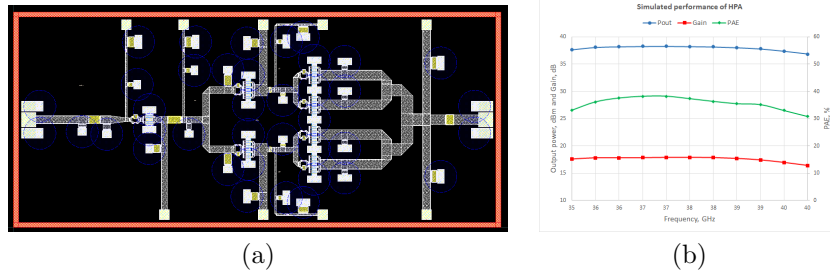


(a)      (b)

Figure 6: Power amplifier involved in the system, layout of the integrated circuit, (a), and simulated performance, (b).

### 5.4. The low noise amplifier

The second sub-system component designed for the specific purpose of the MIMO radar, consists of the low noise amplifier (LNA). This component shall be designed according to the specification of Table 2, in particular the main feature of the LNA regards it linearity with respect to the blocking signals that can interest the radar receiver due to transmitter leakage and short distance reflecting objects. In this case the GaN-HEMT technology appears to be effective due to its inherent good performance in terms of both linearity and low-noise figure, [13]. In Fig. 7a we report the integrated circuit layout of the 3-stage LNA exploiting the same GaN-HEMT device adopted for the PA properly scaled and biased; while in the Fig. 7a–b are shown the small signal and the large signal performance respectively. The LNA is capable to provide 20 dB of gain with a noise figure less than 2 dB acorss the specified bandwidth with an associated output referred 1-dB compression of 25 dBm and 33 dBm of third-order intercept point.
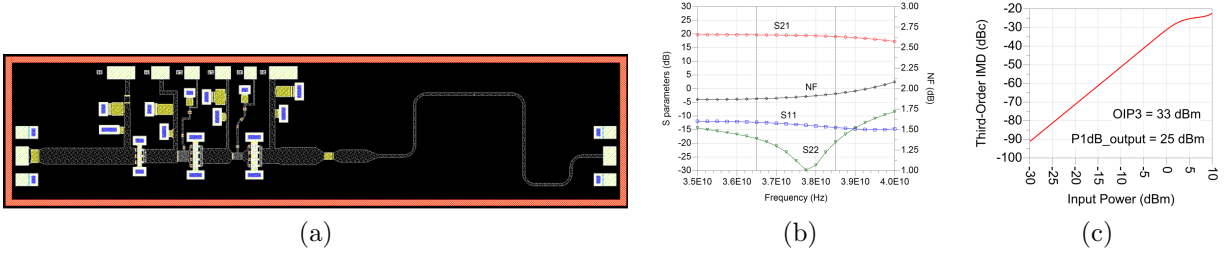
Figure 7: Low noise amplifier involved in the system, layout of the integrated circuit, (a), simulated small signal , (b), and large signal, (c), performance.

## 5.5. The zero-IF mixer

The key feature of the mixer follow those of the LNA in terms of linearity and noise figure. In addition its design is made critical from the frequency conversion operation and the IF bandwidth requirements, which is as low as zero Hz, having to detect echo signals from target potentially very close at the front-end. In addition to the technique described in [14] for the optimization of the RF and IF termination, the required feature makes the mixer of the class of zero-IF and thus requires couplers, baluns and splitters to cancel the spurious signals at the IF output, [15]–[16] . Also for this component we adopted a pair of identical GaN-HEMT properly scaled and biased. In Fig. 8a we report the integrated circuit layout, while the Fig. 8b shows the simulated performance; from the figure we observe the capability to provide few dB of conversion gain, with a local oscillator level of 30 dBm and a rejection of the 2-nd and 3-th order intermodulation product at IF port in excess of 35 and 30 dB respectively across the designed bandwidth. The estimated output noise at the IF port is 10 $nV/\sqrt{Hz}$.
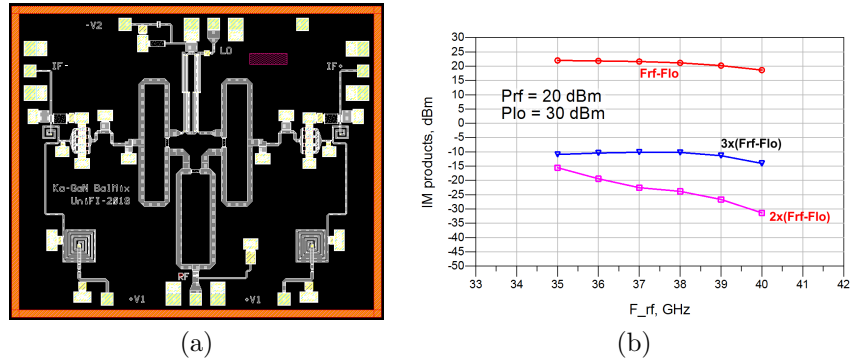


Figure 8: Zero-IF mixer involved in the system, layout of the integrated circuit, (a), simulated large signal performance (b).

## 5.6. The MIMO antenna

An array composed of $M_R = 2$ and $M_T = 2$ antenna was designed fabricated and tested, cf. Fig. 9a. Each antenna element is itself a linear array of patch elements designed with the concept of the series fed patch antenna array [17]–[18] and optimized,[19], for the 12.5 mil plastic laminate Isola–AstraM77. The rational of this design consists in providing the system simulator with the actual characteristics of the antenna and in particular including in the analysis the effect of the TX to RX channels coupling, which is of dramatic relevance for this specific application. In Fig. 9a we see additional feeding lines that were inserted with the aim of the characterization, while in Fig. 9b we see see the coupling between channels that can be in excess of 30 dB. From Fig. 9c we can observe the radiation pattern of the antenna RX # 1: in the vertical plane the antenna exhibits 12 dB of gain and 78 % of efficiency across the design frequency band.

## 6. SYSTEM LEVEL ANALYSIS

In this Section we analyze a case study defined by the set of data reported in Table 1 and Table 2. In this context, a number of system level analysis have been carried out by using a suite composed
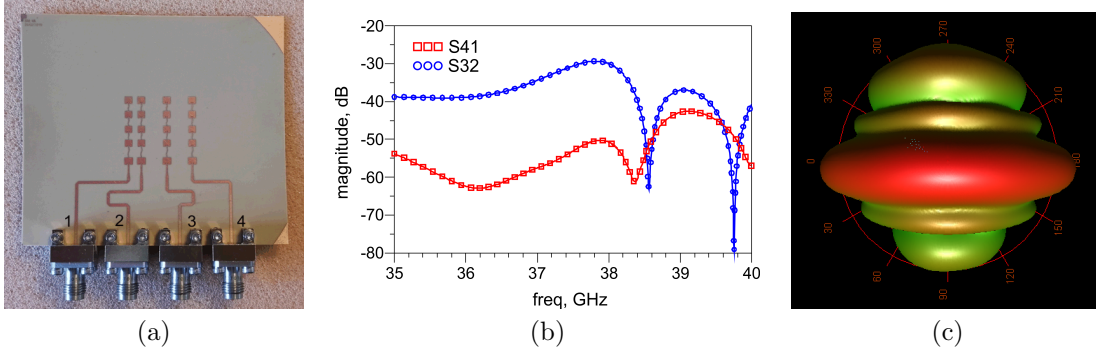
Figure 9: 2x2 MIMO antenna array involved in the system analysis: prototype, (a), isolation between TX and RX ports, (b), radiation pattern of antenna # 1.

of a circuit simulator engine and a system level simulator, capable to integrate co-simulations in the envelope domain and numerical scripts for the signal processing.

The components described in the previous Section, at the exception of the antenna, where characterized in terms of X-parameters behavioral model, [19]–[21] and included in the system simulator. The antenna was included in the simulator in order to define the gain as a function of the angle $\theta$, cfr. Section 4, as well as the coupling between the channels, the latter needs of a matrix of scattering parameters.

Concerning the wideband synthesizer, we refer to a commercially available component that, cascaded with a proper frequency multiplier, is capable to provide about 37.5 GHz, a single side phase noise level of -115 dBc/Hz at 1 MHz offset frequency, which is adequate for the system specifications according to Table 2.
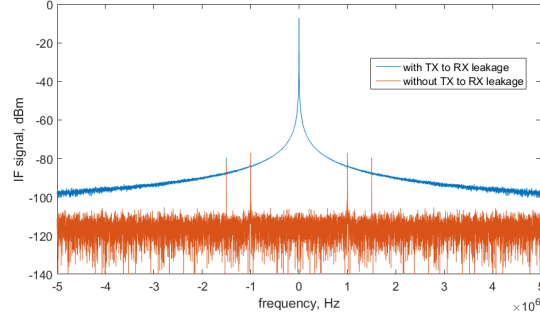


Figure 10: IF signal spectrum corresponding at a TX–RX pair; comparison between the case of both absence and presence of a TX to RX leakage of -50 dB.

The first set of data is related to the range analysis and to a single pair of TX and RX channel. We simulated two targets with the same $\sigma_{av}$ at the distance of 300 and 200 m respectively; they result in an IF spectrum response respectively at 1.5 and 1 MHz. The Fig. 10 shows the comparison between two significant cases. The first consist on the response with the absence of any leakage between the TX and the RX channels, in this case the two tones are above the noise level of more that 30 dB. In the second case the presence of a TX to RX leakage of -50 dB lead to an additional noise-like signal that degrades the IF response and reduces to less than 8 dB the expected SNR at the detector. The broad shape visible in the related trace is to be attributed to the incoherence between transmitted and received chirp signal, rather than the presence of phase noise; indeed the latter is completely removed as observed in the related trace. Thus the first conclusion consists on the relevance of the TX-to-RX leakage, even if the level is within the receiver dynamics.

The second set of results concerns the impact of the virtual array dimension in the MIMO architecture performance, in this set of simulations the signal bandwidth were reduced to 10 MHz in order to make more visible the targets position on the map; for the purpose of this investigation, the reduced bandwidth does not impact on other radar performance. Comparing the two sets of data, in addition to an obvious increase of the cross-range resolution, as it would be expected by the discussion of Section 4, there is a significant impact of the isolation between TX and RX. The
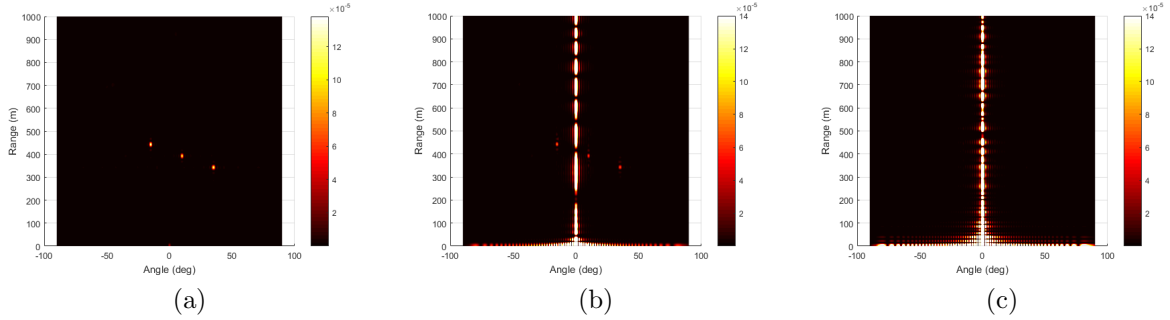
Figure 11: 4x16 MIMO radar image related to 3 identical UAVs, $\sigma_{av} = 0.1m^2$ with different level of TX-to-RX leakage: -70 dB (a), -40 dB (b), -30 dB (c).
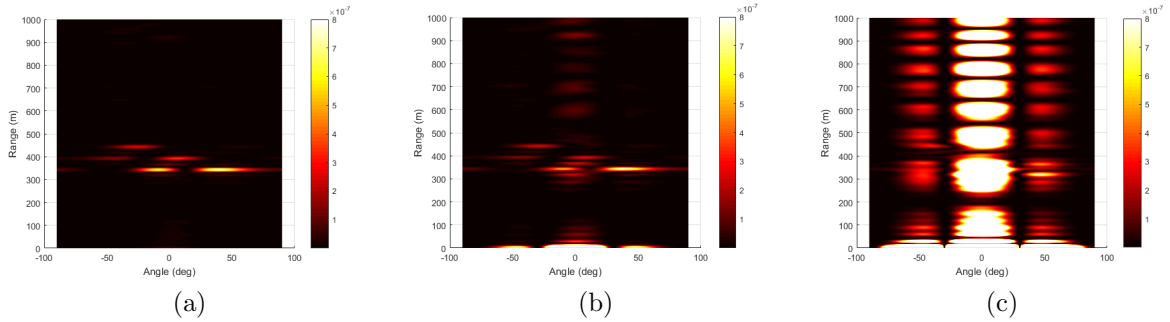


Figure 12: 2x2 MIMO radar image related to 3 identical UAVs, $\sigma_{av} = 0.1m^2$ with different level of TX-to-RX leakage: -70 dB (a), -50 dB (b), -40 dB (c).

Fig. 11 shows radar images in range and angle for a $M_R = 16$, $M_T = 4$ MIMO radar architecture. The figure reports three images of the same scenario, where only the three targets are present, with increasing leakage. From Fig. 11a we can observe that the three targets are distinguished clearly, and no other spurious signals are present, because all the three signals are within the dynamics of the receivers. Moving to Fig. 11b and Fig. 11c, we see that the leakage introduces a blind zone just in the boresight direction, while for angle $\neq 0$ its effect vanishes. If the leakage increase up to -30 dB, which is the case of Fig. 11c, the fringing of the leaked signal, due to the second FFT elaboration discussed in Section 4.1 become more relevant and the targets vanish; actually their signal collapse under the noise level. Moving on the case of $M_R = 2$, $M_T = 2$, whose corresponding images are shown in Fig. 12, we see that the reduced cross-range resolution is significantly lower than the previous case, and also in absence of the leakage (cf. Fig. 12a) the signal lobes manifest themselves as false-targets. The presence of side lobes are related to the FFT processing for the digital beamforming (cfr. Section 4.1) and they become visible because their amplitude is not neglectable with respect the main lobe as in case of Fig. 11a, thus a significant post-processing is required to distinguish actual targets from false signals. In addition to this effect, the present case exhibits more weakness with respect to the $M_R = 16$, $M_T = 4$. In fact, as the isolation reduces below -50 dB the IF signals enriches of a large component about $angle \approx 0$ and compress the echo signal close to the noise floor, simultaneously the lobes of the leakage and echo interfere making the radar image not longer suitable for target detection.

A second conclusion arises from these results: assuming the signal received at the radar front-end within the receiver dynamic range, the increase of MIMO virtual elements increases the immunity to TX-to-RX leakage.

## 7. CONCLUSION

This work has dealt with the system level analysis of a MIMO radar for the detection of small UAVs. We have reviewed the operation principles of both the conventional FMCW radar and the MIMO architecture, with the aim of providing to the reader the required knowledge of the sources of the major impairments in these specific applications. The system considers a front-end developed around the GaN-HEMT monolithic microwave integrated circuit technology, and specifically included in the simulations the large-signal X-parameters based models for the PA, the

LNA and the mixer, which were designed for the specific application, at the center frequency of 37.5 GHz and with 1.5 GHz of bandwidth. The budget link analysis provided a set of specifications that have been verified in a more detailed system level analysis conducted by using a commercial system level CAD. In addition to the verification that the designed circuits are suitable for the integration in a MIMO radar, and that are capable to provide the required performance, we have investigated the impact of the leakage between the TX and RX channels. It resulted that the MIMO architecture is capable to remove this impairment up to a given extent, provided that the signals remain within the front-end dynamic range.

**ACKNOWLEDGMENT**

**REFERENCES**

1. Brooker, G. M., Understanding millimetre wave FMCW radars, in *1st International Conference on Sensing Technology*, Palmerston North, New Zealand, November, 2005, 152–157.

2. Chen, V. C., Li, F., Ho, S.-S., and H. Wechsler, Micro-doppler effect in radar: phenomenon, model, and simulation study, *IEEE Tran. Aerospace and Electronic Sys.*, Vol. 42, No. 1, pp. 2–21, 2006.

3. M. Pieraccini, L. Miccinesi, CWSF Radar for Detecting Small UAVs, 2017 IEEE Conf. Microw., Antennas, Comm. and Elect. Systems, COMCAS, Nov. 2017

4. Cidronali, A., Maddio, S., Passafiume, M., and Manes, G. "'Car talk: Technologies for vehicle-to-roadside communications"', *IEEE Microwave Magazine*, Vol. 17, No. 11, 40-60, 2016.

5. Maddio, S., Cidronali, A. and Manes, G., "Real-time adaptive transmitter leakage cancelling in 5.8-GHz full-duplex transceivers." *IEEE Trans.s on Microw. Theory and Tech.* Vol. 63 No. 2, 509–519, 2015.

6. Fishler, E., Haimovich, A., Blum, R., Chizhik, D., Cimini, L., and Valenzuela, R., "MIMO radar: An idea whose time has come" in *Proceedings of the IEEE radar conference*, Philadelphia, PA, USA, April 2004, 71-78.

7. Zankl, D., Schuster, S., Feger, R., and Stelzer, A."What a blast!: A massive MIMO radar system for monitoring the surface in steel industry blast furnaces", *IEEE Microwave Magazine*, Vol. 18, No. 6, 52–69 (2017).

8. Feger, R., Wagner, C., Schuster, S., Scheiblhofer, S., Jager, H., and Stelzer, A., "'A 77-GHz FMCW MIMO radar based on an SiGe single-chip transceiver", *IEEE Trans. on Microw. Theory and Tech.*, Vol. 57, No. 5, 1020-1035, 2009.

9. Huang, Y., Brennan, P. V., Patrick, D., Weller, I., Roberts, P., and Hughes, K., "FMCW based MIMO imaging radar for maritime navigation" in *proceedings of Progress In Electromagnetics Research*, Vol. 115, No. 4, 327–342 2011.

10. Camarchia V., Quaglia R., Ramella C., Pirola, M., "Power amplifier MMICs for 15 GHz microwave links in 0.25 um GaN technology", in *Proc. Int. Workshop Integrated Nonlinear Microw. Millimetre-Wave Circ.INMMiC 2017*, n. 792731, 2017.

11. Giofre' R., Colantonio P., Giannini F., Ramella C., Camarchia V., Iqbal M., Pirola M., Quaglia R., "A comprehensive comparison between GaN MMIC Doherty and combined class-AB power amplifiers for microwave radio link", *Int. J. Microw. Wireless Technol.*, vol. 8, n. 4-5, pp. 673-681, 2016.

12. Cipriani,E., Colantonio, P. and Giannini, F. Ka-Band GaN-on-Si 4 W MMIC High Power Amplifier for Millimetre-wave Radar, in *Proceeding of 2018 IEEE Topical Conference on Power Amplifiers for Wireless and Radio Applications (PAWR)*, Orlando, Florida, Jan. 2018.

13. Suijker, et al. "'Robust AlGaN/GaN low noise amplifier MMICs for C-, Ku-and Ka-band space applications", In *Proceeding of 2009 Annual IEEE Compound Semiconductor Integrated Circuit Symposium*, Greensboro, NC, USA, October 2009.

14. Cidronali, A., Gupta, K.C., Jargon, J., Remley, K.A., DeGroot, D., Manes, G., "Extraction of conversion matrices for P-HEMTs based on vectorial large-signal measurements", in *Proceedings of IEEE MTT-S International Microwave Symposium Digest* pp. 777-780. Philadelphia, PA; USA, 8–13 June 2003

15. Avitabile, G.F., Cidronali, A., Salvador, C., Speciale, M., "Compact MMIC 90 coupler for ISM applications", in *Proceedings of IEEE MTT-S International Microwave Symposium Digest*, 281-284. Denver, CO, USA; 8–13 June 1997

16. Cidronali, A., Nair, V., Collodi, G., Lewis, J.H., Camprini, M., Manes, G., Goronkin, H., "MMIC applications of heterostructure interband tunnel devices" *IEEE Trans. on Microw. Theory and Tech.*, Vol. 51 No.4, 1351-1367, 2003.

17. Singh, B., Sarwade, N., and Ray,K. P. "'Compact series fed tapered antenna array using unequal rectangular microstrip antenna elements,"' *Microwave and Optical Technology Letters*, Vol. 59, no. 8, 1856–1861, 2017.

18. Maddio, S., Pelosi, G., Righini, M. and Selleri, S. "A compact series array for vehicular communication in the c-band,"' in *2019 IEEE International Symposium on Antennas and Propagation & USNC/URSI National Radio Science Meeting.* IEEE, 2019, IN PRESS.

19. Agastra, E., Pelosi, G., Selleri, S. and Taddei, R., "'Taguchi's method for multi-objective optimization problems," *International Journal of RF and Microwave Computer-Aided Engineering*, Vol. 23, no. 3, 357–366, 2013.

20. Root, D. E., Verspecht, J., Horn, J., and Marcu, M. "X-Parameters: Characterization, Modeling, and Design of Nonlinear RF and Microwave Components" Cambridge University Press, 2013.

21. Casini, G., Cidronali, A., Manes, G., "Investigation of X-parameters modeling for accurate envelope tracking power amplifier system simulations" in *Proceedings of IEEE MTT-S International Microwave Symposium*, Seattle, WA, USA, 2-7 June 2013